06

Study of the structure of powdered nanocelluloses isolated from industrial waste using X-ray diffraction and computer modeling methods

© A.I. Prusskii,[1] O.V. Tokko,[1] A.V. Kadetova,[1] N.E. Kotelnikova,[2] V.V. Kiselev[1]

[1] Petrozavodsk State University,
185035 Petrozavodsk, Russia
[2] Branch of the Federal State Budgetary Institution Petersburg Nuclear Physics Institute named after B.P. Konstantinov of National Research Centre „Kurchatov Institute“, — Institute of Macromolecular Compounds,
199004 Saint Petersburg Russia
e-mail: solvak@yandex.ru

Received August 2, 2025
Revised September 26, 2025
Accepted November 21, 2025

Structural studies of powder samples of nanocellulose (NC) isolated from waste paper (newsprint and cardboard waste) were performed for the first time. It was established that the structure of the NC samples corresponds to the antiparallel model of cellulose $I\beta$. The degree of crystallinity of the samples determined by the modified Ruland method was $\sim 64\,\%$, which is lower than similar indicators of powder celluloses isolated from fibrous waste of plant celluloses, namely flax fiber and bleached hardwood cellulose. The largest size of the coherent scattering region (CSR) was observed along the fibril growth axis [001], indicating an elongated morphology of the crystallites. Using computer modeling, it was shown that the correspondence between the experimental and theoretical scattering curves is achieved by superposition of several types of clusters with different levels of ordering.

Keywords: natural polymers, X-ray structural analysis, CSR, degree of crystallinity, computer modeling.

DOI: 10.61011/TP.2026.02.62885.196-25

Introduction

Being a natural polysaccharide, cellulose is the main structural component of plant cell walls and a promising material due to its unique properties: availability, renewability, sustainability, flexural strength, biodegradability, hygroscopic properties, etc. [1,2]. Cellulose-based materials are currently widely used in 3*D*-printing, photonics, catalysis, energy storage and generation, in electronics and pharmaceutical industry [3]. They are also used in biomedicine as a carrier for delivery of drugs and in tissue engineering for wound healing. Biodegradability and easy composting make cellulose a promising material for creating environmentally friendly technologies and for waste reduction [1,4].

Permolecular structure of cellulose is treated as a combination of various structural forms, which differ in properties: crystalline, amorphous and nanocrystalline [5]. Cellulose crystal structure plays a key role in defining physical properties of materials. Crystalline regions are formed due to close-packed chains formed by $\beta-D$-glucopyranose units, offering high mechanical strength, rigidity and stability of material [5]. Crystalline cellulose can exist in the form of microfibers, nanofibers and nanocrystals [6]. Parameters of various crystalline cellulose forms depend on the natural origin of cellulose, extraction method and post-treatment [4].

Amorphous cellulose regions have a disordered structure, which reduces mechanical strength, but increases flexibility of cellulose [7,8]. Amorphous cellulose is obtained by solution recovery, for example, in SO_2-DEA$-$DMSO system [7], DMAA/LiCl solvent system and others [9]. Amorphous structure of regenerated celluloses was confirmed using the X-ray diffraction analysis (XRD), infrared (IR) spectroscopy and differential scanning calorimetry (DSC) [7,8].

In recent years, nanocrystalline cellulose (NC) produced through acid hydrolysis of cellulose and cellulose esters [10] has become an important intermediate material for hi-tech products. It features high rigidity, strength, light weight, dimensional stability and adjustable surface properties [11]. NC crystalline form is generated by nanocrystals with different morphology: rods, spheres and cross-linked structures [10]. Acid hydrolysis parameters such as acid concentration, temperature and reaction time influence the nanocrystal size and shape, offering targeted variation of their properties and wider understanding of nanostructured cellulose material formation mechanisms [12].

Spectral and thermal analysis methods are used to study cellulose structure. XRD is used to determine the degree of crystallinity and phase composition of the studied samples [8]. Functional composition of samples is identified using the IR spectroscopy. DSC investigates thermal effects associated with phase transitions in cellulose materials [7,12]. Combination of spectral techniques and computer simulation of atomic configuration provides deeper understanding of molecular arrangements of cellulose samples, which is important for applications.

Cellulose, which is the base component for producing NC, its derivatives and composite materials, is generally obtained from various natural sources. However, cellulose

can be obtained from industrial waste [11], in particular, paper products (newspapers, magazines, cardboard) [13].

This work used NC samples, which were first extracted from deinked pulp (DIP), waste newspapers and cardboard, as the objects of study. NC samples were distinguished by extraction techniques that were purpose-built for such type of feedstock using high-concentration inorganic acids.

The aim of this study was to perform structural investigation of NC samples extracted from DIP and computer simulation of their atomic structure. Identifying similarities and differences in the structure of nanocellulose samples of various origin is important for planning their potential future use. Besides the scientific and practical aspects of study, using NC from industrial waste has prospects from environmental considerations [14].

1. Samples and methods

1.1. Preparing nanocellulose samples

Powder nanocellulose samples NC-1 and NC-2, obtained from waste paper were examined. Mixed DIP (waste newspapers and cardboards) was used for NC extraction. Waste paper processing consisted of two key phases: pretreatment and acid hydrolysis of DIP as described by Mikhailidi et al [9]. Unlike previous studies, acid hydrolysis of pretreated samples was carried out in H_2SO_4 and HCl solutions in a wide range of concentrations. Two base experiments providing the best results are briefly described below:

1) sulphuric acid hydrolysis: fiber sample NC-1 was put into 55% H_2SO_4 solution, the mixture was stirred in a magnetic stirrer at T 40 °C–50 °C during 1.5 h. After cooling, dilution with distilled water with ratio of 1 : 50 and filtration using a glass filter, a powder sample was separated, washed to neutral reaction and air-dried;

2) hydrochloric acid hydrolysis: fiber sample NC-2 was placed in 4M HCl solution. Reaction was carried out at T 40 °C with continuous stirring during 2.5 h. The obtained mixture was diluted with distilled water with ratio of 1 : 30, filtered using a glass filter, washed to neutral reaction and air-dried.

1.2. XRD

X-ray patterns of the studied samples were made using the DRON type diffractometers (in CuK_α ($\lambda = 1.54178$ Å) and MoK_α ($\lambda = 0.7307$ Å) radiations) in two geometries: reflection-based (Bragg geometry) and transmission-based (Laue geometry) at the scattering angles 2θ from 2° to 60° with a step of 0.1° and from 60° to 145° with a step of 0.2°. Stable operation of the diffractometer was controlled by scattering measurement using a standard before and after obtaining each diffraction pattern of a sample.

Crystallinity degree (CD) of cellulose was calculated using the Ruland method [15–17] at the scattering angles 2θ from 7° to 30° (CuK_α) as follows:

$$\mathrm{CD} = (I - I_{am})/I, \tag{1}$$

where I is the total integral scattering intensity of crystalline and amorphous phase calculated as an area under the entire experimental curve:

$$I = \int_{2\theta_1}^{2\theta_2} I(2\theta_i)d(2\theta);$$

I_{am} — integral scattering intensity of amorphous phase:

$$I_{am} = \int_{2\theta_1}^{2\theta_2} I_{am}(2\theta_i)d(2\theta).$$

Positions of the initial and end points of the background and maximum peaks were determined by the first and second smoothed derivatives. The contours of the reflections and the maximum of diffuse scattering by the amorphous phase were approximated by Gaussian functions. Amorphous maximum in the X-ray pattern of cellulose is caused by molecular fragment disordering [18–22]. For details of the modified Ruland method, see [16,23].

Sizes of the crystallinity areas D_{hkl} (mosaic blocks, coherent scattering regions (CSR)) were calculated using the Scherrer equation [16,19–22] on the basis of broadening of reflection (β_{hkl}) in the X-ray pattern in two approximations, Cauchy and Gauss, respectively. Real CSR sizes are within the values obtained in these approximations [24], the obtained values are averaged for further analysis. CSR sizes obtained in the [1$\bar{1}$0], [110] and [100] directions of the cellulose lattice were used to determine the shape and cross-sectional area of elementary fibrils.

Characteristics of the crystalline component of cellulose samples were refined using the Rietveld method ($\mathrm{PDW_{in}}$ software) [25]. The method is based on minimizing the functional Φ [26]:

$$\Phi = \sum_{i=1}^{N} w_i[(I_i^{exp} - I_i^{teor})]^2, \tag{2}$$

where I_i^{exp} and I_i^{teor} are experimental and theoretical scattering intensities in each diffraction pattern point from $i = 1$ to N, w_i is the weight coefficient.

Experimental scattering intensities were converted into electronic units, then curves of s-weighted interference function $H(s)$ and pair function distribution $D(r)$ were calculated by the Finback–Warren method [27–29]. Short-range order characteristics were determined from curves $D(r)$: N_{ij} are the coordination numbers (least-square method (LSM)), and r_{ij} are the coordination sphere radii and σ_{ij} are their blurring (method of successive approximations) [19].

The obtained data were used to calculate the pair function curves $D_{\mathrm{LSM}}(r)$, which were compared with experimental

curves $D(r)$. Validity of the obtained values was estimated by the degree of coincidence of experimental and theoretical data.

1.3. Atomic-molecular configuration technique for cellulose

Short-range ordering structure of the cellulose samples was described using the computer simulation method. Earlier in [27,30,31], this method was successfully implemented for modified cellulose samples.

The first stage of constructing configurations consists of obtaining the initial model of the cellulose crystallite by translation the unit cell along the crystallographic axes whose periods and angles were refined for each sample by the Rietveld method. The number of translations in this work varied from 1 to 10 in all crystallographic directions.

„Amorphization" of the built clusters was performed in HyperChem8, i.e. using the Polak−Ribiere method (molecule geometry optimization) and molecular dynamics (MD) method, with force potential MM+, the maximum number of steps was up to 8000 [32,33].

Diffraction model curves $I_{mod}(s)$ were calculated by the modified Debye method, method of disoriented clusters [34], which were used to calculate $H_{mod}(s)$ and radial atom distribution functions characterizing the atom distance distribution probability,

$$W_{mod} = \frac{D_{mod}(r)}{D_0(r)} \text{ [27].}$$

Since curve $H_{mod}(s)$ is more contrast compared with $I_{mod}(s)$, it was visually compared with the experimental curve $H_{exp}(s)$. Curves $H_{mod}(s)$ were calculated both for CuK_α (for better resolution) and MoK_α (to extend the reciprocal space). For contrast enhancement, the scattering pattern of $H_{mod}(s)$ was built as follows: values for measurement were taken before and after $4\,\text{Å}^{-1}$ using CuK_α and MoK_α, respectively.

Moreover, adequacy of the proposed model was estimated by the profile uncertainty factor R_p:

$$R_p = \frac{\sum\limits_k [I_{exp}(s) - I_{mod}(s)]}{\sum\limits_k I_{mod_k}(s)}. \quad (3)$$

In case when model cluster deformation was necessary, possibility to remove chains in the ab plane was implemented. Thus, a „void" within a model cluster was formed. This technique was used in [31] to determine the structure of cellulose nitrate from miscanthus sacchariflonis.

To describe a real cellulose object for computer simulation, due consideration was made of the fact that cellulose morphology could be described by superposition of clusters having different size and deformation.

The distribution curve of model scattering intensity was calculated taking into account concentration of each type of clusters. The following equation was used for calculating the model scattering intensity:

$$I_{mod}(s) = \sum_i I^i_{mod}(s) \cdot c^i, \quad (4)$$

where $I^i_{mod}(s)$ is the model curve of scattering intensity distribution by the i-th cluster, c^i is the concentration of the i-th cluster in the final model, i is the cluster number.

2. Results and discussion

2.1. X-ray pattern analysis

Figure 1 shows intensity distribution curves $I(s)$ obtained reflection and transmission geometry with CuK_α radiation for samples NC-1 and NC-2.

These curves are compared with the theoretical X-ray pattern built for cellulose $I\beta$ model with antiparallel molecular arrangement [35], and with X-ray patterns of previously studied powder celluloses obtained from linen fiber (LC) and bleached hardwood cellulose (HC) using the acid hydrolysis [36]. Reflection indices are given for cellulose $I\beta$.

When comparing scattering patterns for powder samples NC-1 and NC-2 obtained from waste paper (curves *1* and *2*) with samples obtained LC (curve *3*) and HC (curve *4*) waste fibers, it can be seen that X-ray patterns of the cellulose samples are generally similar. However, there are some differences. Thus, maxima of reflections from the $(1\bar{1}0)$ and (110) planes are clearly resolved in LC scattering patterns obtained in two geometries. They form a single maximum on the experimental curves of samples NC-1, NC-2 and HC due to the presence of the amorphous component in the powder cellulose samples. LC sample has higher intensity of the base maxima.

Generally, scattering intensity distribution curves $I(s)$ built for both samples NC-1 and NC-2 correlate with each other and with the theoretical pattern built for cellulose $I\beta$ [35]. However, there is a difference in intensities on curves $I(s)$ obtained in different measurement geometries. In addition, on curve $I(s)$ obtained for sample NC-2 in the transmission geometry (Figure 1, *b*), maximum (004) corresponding to $s \sim 2.4\,\text{Å}^{-1}$ is higher than on the curve built for sample NC-1 (Figure 1, *b*). As mentioned above, this reflection characterizes the elementary fibril length.

Similar differences between the scattering curves obtained in reflection and transmission geometries are also observed for samples LC and HC [36] (Figure 1).

These differences in curves $I(s)$ obtained in different measurement geometries indicate that there is structure anisotropy of the cellulose samples, which is confirmed by the literature data [8]. Moreover, Figure 1 shows that the most intense reflection (200) on the experimental curves of the studied samples is shifted towards smaller angles with respect to the theoretical $I\beta$ cellulose scattering curve [35].

Rietveld method was used to find that the structure of the studied samples corresponded to phase $I\beta$.

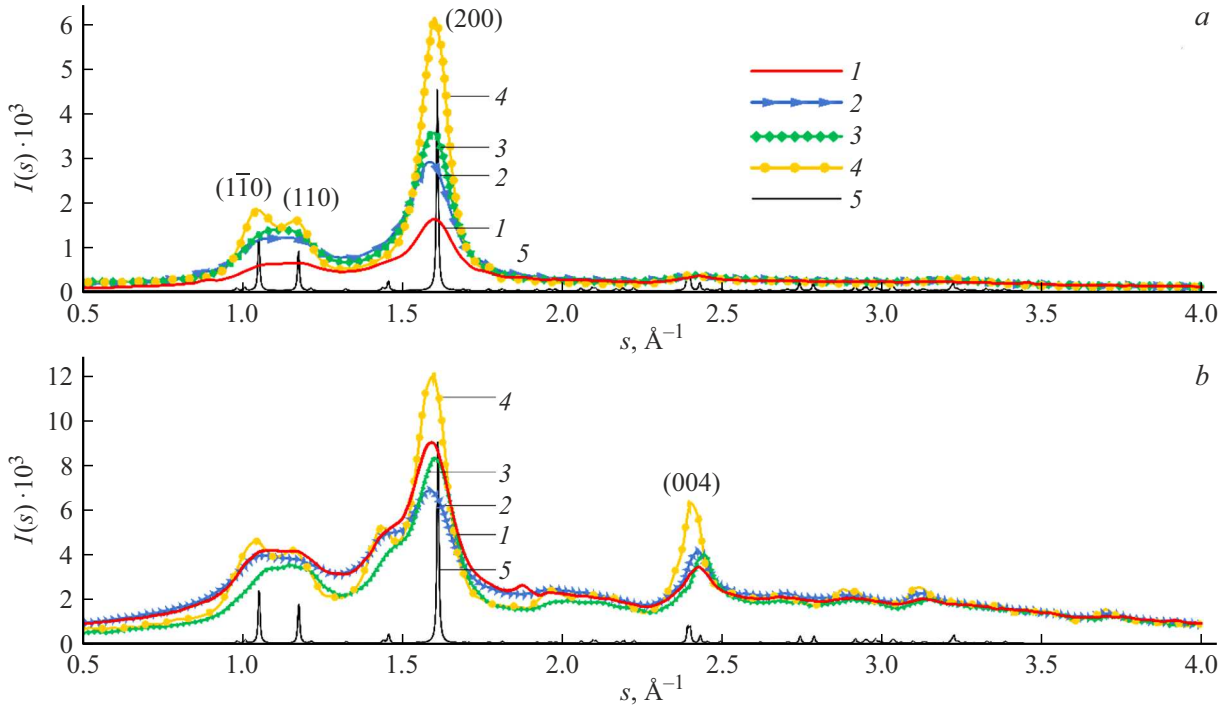

Figure 1. Comparison of intensity distribution curves $I(s)$ obtained during the reflection-based measurement (a) and transmission-based measurement (b): *1* — NC-1; *2* — NC-2; *3* — HC [36]; *4* — LC [36] with theoretical X-ray pattern of cellulose $I\beta$ (*5*) [35].

Table 1. Refined unit cell parameters and volumes of samples NC-1 and NC-2 compared with the data for cellulose phase $I\beta$ [35]

	a, Å	b, Å	c, Å	γ, °	V, Å^3	$T_{1\bar{1}0}$	Rp, Rw,%
Phase $I\beta$ [35]	7.846	8.171	10.34	96.38	658.789	–	–
NC-1	7.9291(2)	8.0381(8)	10.276(2)	96.15(2)	651.(2)	1.185	4.45, 5.82
NC-2	7.9350(2)	8.1099(8)	10.174(1)	96.39(2)	651.(2)	1.029	5.44, 8.07

Note. T is the parameter of axial texture with the $\{1\bar{1}0\}$ axis and Rp, Rw are the profile and weight uncertainty factors.

Analysis of the refined unit cell parameters and volumes listed in Table 1 compared with the values for cellulose phase $I\beta$ [35] has shown that the shift of reflection (200) on the X-ray pattern of samples (Figure 1) was caused by a decrease in unit cell parameter b and an increase in parameter a.

Table 2 shows permolecular structure characteristics for samples NC-1 and NC-2: CD value and size of CSR. Values of D_{004} are given only for the transmission measurement due to anisotropic structure of the studied samples.

CD for samples NC-1 and NC-2 was (64 ± 5) %. Compared with these results, samples LC and HC [36] had much higher content of the crystalline component by ~ 25 % and ~ 11 %. The obtained result shows that the choice of feedstock and recycling method affects the cellulose structure ordering.

CSR sizes (D_{hkl}) in the [110], [100] and [1$\bar{1}$0] directions for powder samples NC-1 and NC-2 vary insignificantly (Table 2), the size and shape of the cross section are correlated (Figure 2).

CSR sizes in the [102] direction calculated for sample NC-1 is larger by 17 Å than that for sample NC-2. Maximum CSR sizes for both samples are observed along the [001] direction, suggesting that the crystals are elongated along the fibril growth axis: $D_{004} = 80$ Å for sample NC-1, $D_{004} = 103$ Å for sample NC-2. CSR sizes in the [001] direction is larger by 24 Å than that of sample NC-2, suggesting that elementary fibrils are longer.

Comparison with previously studied samples LC and HC has shown that the largest CSR sizes are observed for the linen powder cellulose sample [36] in the $[hkl]$ directions, which characterize the cellulose fibril cross-sections: [1$\bar{1}$0] and [110] — along the unit cell basal plane diagonals; [100] — along the a axis. D_{hkl} of sample LC along the [1$\bar{1}$0] direction is larger by 32 % than that of sample HC, by 28 % than that of sample NC-2, and by 19 % than that of sample NC-1; along the [100] direction is larger by 23 % than that of sample HC, by 27 % than that of sample NC-2, and by 31 % when compared with sample NC-1. In the [110] direction, difference in D_{110} for all given samples is within the acceptable error.

Table 2. Reflection-averaged and transmission-averaged CD

Sample	NC-1					NC-2				
X-ray diffraction geometry	Reflection-based		Transmission-based		average	Reflection-based		Transmission-based		average
CD, %	64.3					64.5				
D_{hkl}, Å	g	k	g	k	$\langle D \rangle$	k	g	k	g	$\langle D \rangle$
$(1\bar{1}0)$	38	42	34	38	38	34	37	31	34	34
(110)	49	56	58	68	58	49	56	58	69	58
(102)	57	68	57	68	63	43	49	43	48	46
(200)	43	48	38	42	43	43	48	43	48	46
(004)*	–	–	72	88	80	–	–	90	117	103

$\Delta \mathrm{CD} = \pm 5\,\%; \quad \Delta D_{hkl} = \pm 5\,\text{Å}$

Note. hkl are indices of reflections, whose widths were used to calculate CSR sizes (D_{hkl}); g — Gauss method, k — Cauchy method; $\langle D \rangle$ — average CSR sizes (Gauss−Cauchy).

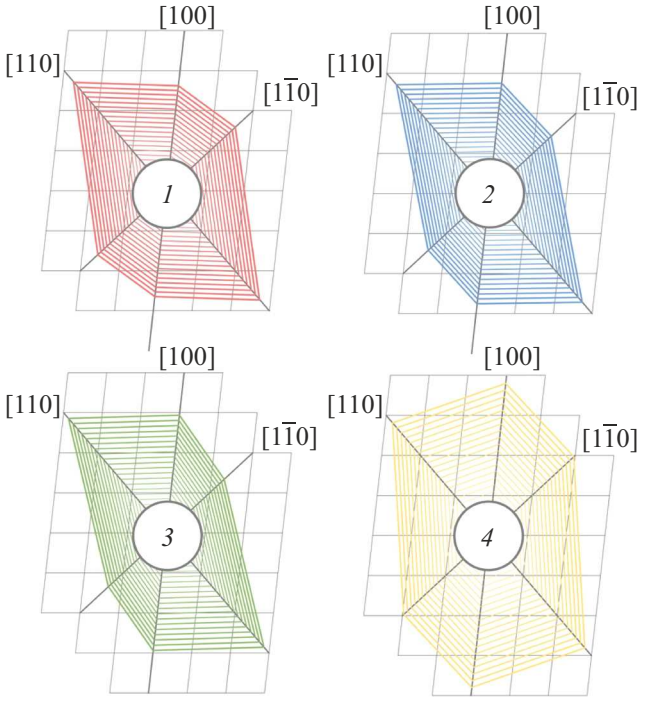

Figure 2. Schematic diagrams of the cross-sectional shape of elementary fibrils NC-1 (*1*) and NC-2 (*2*) studied in this work compared with samples HC (*3*) and LC (*4*) [36].

In the [001] crystallite fibril axis direction, the highest value of D_{001} is also observed for sample LC. The greatest difference in CSR is observed in this direction: D_{004} for LC is larger by 42 % than D_{004} for HC, by 34 % for sample NC-2 and by 48 % for sample NC-1. Difference in D_{004} for samples LC and NC-1 is 75 Å, which approximately corresponds to seven periods of translation along the c axis.

Cross-section shapes of elementary fibrils in unit cell plane ab (Figure 2) of the studied samples are characterized by hexagonal symmetry. The largest area is observed for sample LC, this value is approximately 1.4 times larger than the areas calculated for samples NC-1 (1270 Å^2) and NC-2 (1218 Å^2).

These cross-section areas correspond to $\sim 20 \cdot S_{ab}$ for NC-1 and $\sim 19 \cdot S_{ab}$ for NC-2 (S_{ab} is the unit cell area of cellulose $I\beta$ [35] in plane ab ($S_{ab} = 63.5$ Å^2). Area difference is 52 Å^2 ($0.6 \cdot S_{ab}$).

In addition, the shape of cross-section diagrams of samples HC, NC-1 and NC-2 is „elongated“ along the [110] direction, and sample LC characterized by the highest CD has a diagram shape „elongated “ along the [100] direction, which corresponds to the direction of a axis in the unit cell. This value of D_{200} for sample LC is larger by ~ 27 Å than that for other samples, which corresponds to ~ 3.4 parameter a of the unit cell.

On curves of pair function distribution $D(r)$ (Figure 3, a) and radial distribution function $W(r)$ (Figure 3, b), two maxima are observed at $r \sim 1.5$ and ~ 2.6 Å both for sample NC-1 and sample NC-2, which corresponds to radii of the first and second coordination spheres in the molecule of cellulose $I\beta$ [35] (Figure 4). Intensity of these maxima is different, which suggests that there are differences in the short-range order of two samples, i.e. different values of the first two coordination numbers N_{ij}.

When $r > 3.5$ Å curves $D(r)$ (Figure 3, a) start oscillating along straight line $D_0(r)$, and curves $W(r)$ start oscillating along $W(r) = 1$. Positions of maxima $W(r)$ correspond to the most probable interatomic distances — coordination sphere radii r_{ij}. Width of maxima is defined by the interatomic distance dispersion σ_{ij}. Oscillations on curve $W(r)$ are quickly attenuated and are almost damped at $r = 3.5$ Å. As r grows, any distances between atoms become equally probable, i.e. $W(r) = 1$.

Table 3 shows short-range order characteristics calculated from curves $D_{\mathrm{LSM}}(r)$ in comparison with theoretical values

Table 3. Short-range order characteristics of samples NC-1 and NC-2

Type of sphere	Cellulose $I\beta$		NC-1			NC-2		
	$r_{ij(theor)}$, Å	$N_{ij(theor)}$, at.	r_{ij}, Å	N_{ij}, at	σ_{ij}, Å	r_{ij}, Å	N_{ij}, at	σ_{ij}, Å
C–O_1	1.46	2.6	1.48	2.0	0.35	1.46	1.7	0.28
C–O_2	2.37	2.3	2.38	2.5	0.20	2.38	2.6	0.22
C–C	2.50	1.6	2.60	4.1	0.10	2.53	3.0	0.05
O–O	2.86	3.2	2.90	3.3	0.10	2.85	3.5	0.13
C–O_2	3.02	2.5	3.30	2.0	0.20	3.20	2.5	0.35
C–O_3	3.61	2.1	3.61	3.4	0.10	3.61	3.8	0.05

$\Delta r_{ij} = \pm 0.01$ Å, $\Delta N_{ij} = \pm 0.1$

Note. r_{ij} is the coordination sphere radius, N_{ij} is the coordination number.

for the model of cellulose $I\beta$ with antiparallel molecular arrangement [35].

Values of r_{ij} for NC-1 and NC-2 correspond to those in the model of cellulose $I\beta$ (Table 3). Coordination number $N_{C\text{–}O_1}$ for a coordination sphere with $r_{C\text{–}O_1} \sim 1.46$ Å is lower by $\sim 30\%$ for sample NC-2 and by 20% for sample NC-1 compared with those for cellulose $I\beta$. The third coordination sphere ($r_{C\text{–}C} \sim 2.5$ Å) is characterized by the inverse relation: $N_{C\text{–}C}$ is 1.5 times higher for sample NC-1 and 1.2 times larger for sample NC-2 compared with the theoretical value for the model. This difference in redistribution of coordination numbers is also observed on curves $W(r)$ (Figure 3, *b*).

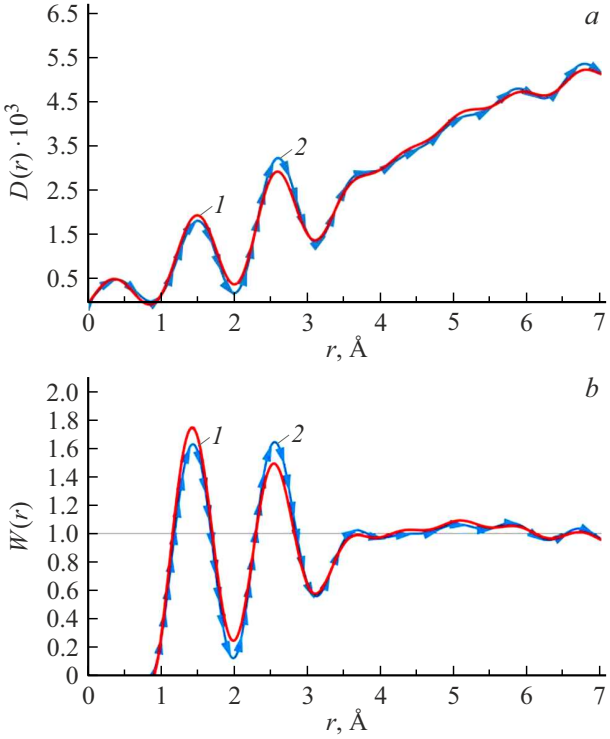

Figure 3. Pair functions $D(r)$ (*a*) and radial atom distribution functions $W(r)$ (*b*) built for samples NC-1 (*1*) and NC-2 (*2*).

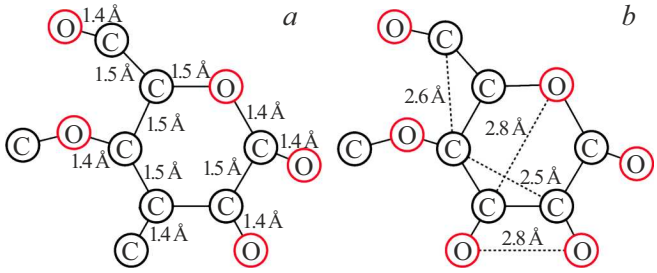

Figure 4. Schematic diagram of cellobiose ring [35]: *a* — the first coordination sphere, *b* — the second coordination sphere.

2.2. Analysis of atomic clusters

2.2.1. Sample NC-1

Data in Table 2 show that crystallite size in samples NC-1 and NC-2 is equal to ~ 5–6 elementary translations along period *a*, ~ 4 — along *b* and ~ 8–11 — along *c*. Refined unit cell parameters are shown in Table 1.

Computer simulation method was used to build atom clusters. Cluster with the translation number 6**a**4**b**8**c** is shown in Figure 5. This cluster contains 16 416 atoms, which corresponds to 194 unit cells ($\sim 776 \cdot (C_6O_5H_{10})$). For this cluster, curves $I_{mod}(s)$ and $H_{mod}(s)$ were built and

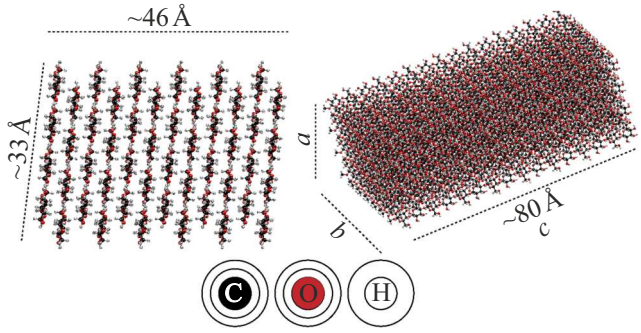

Figure 5. Cluster of cellulose $I\beta$ model [35] with parameters 6**a**4**b**8**c**.

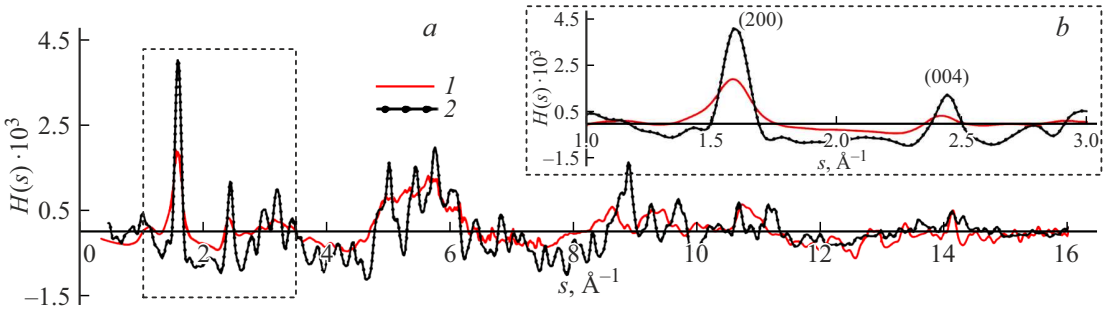

Figure 6. s-weighted interference functions $H(s)$ for NC-1 (*1*) and for cluster **6a4b8c** (*2*).

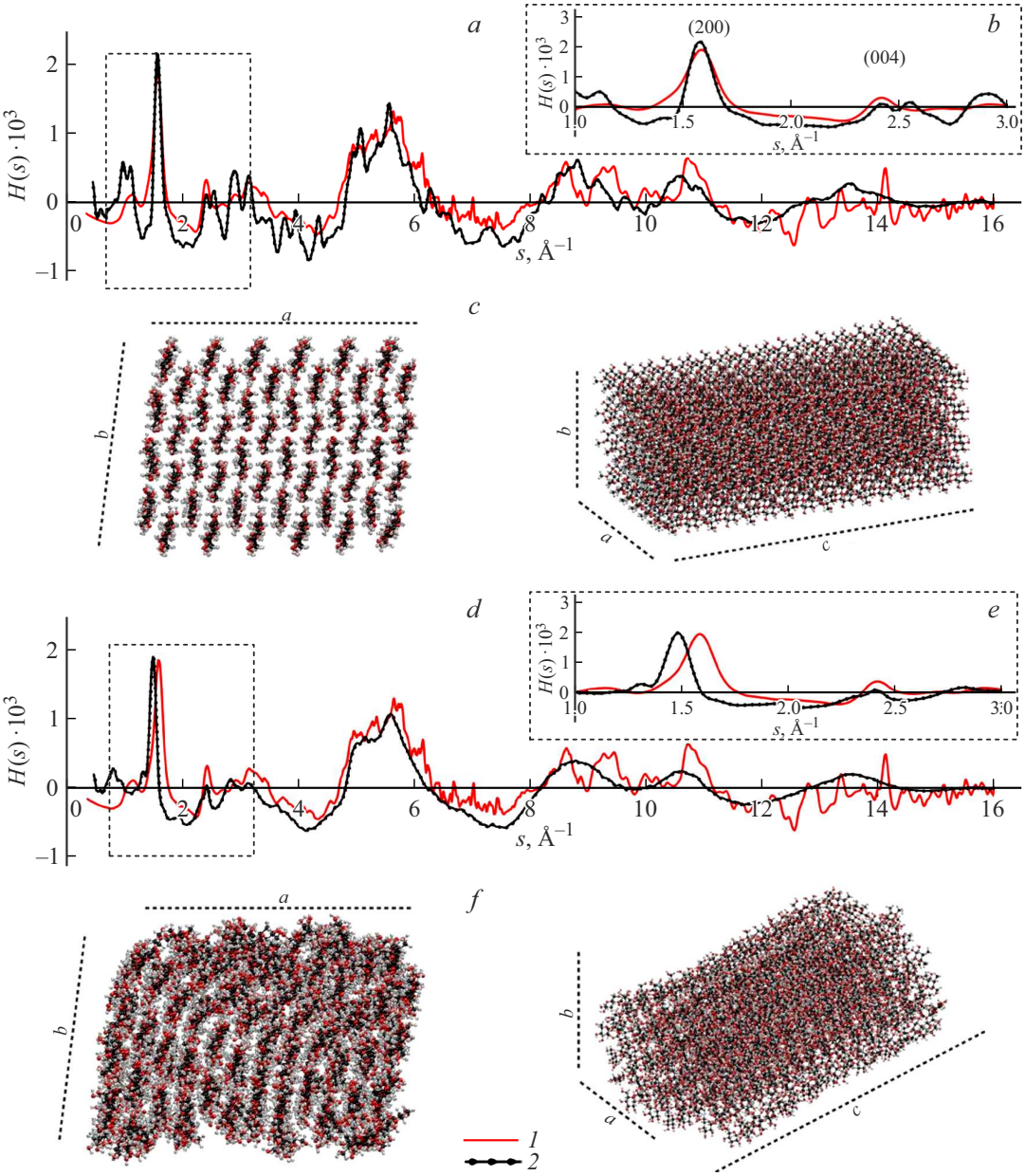

Figure 7. Comparison of curve $H_{exp}(s)$ (*1*) built for NC-1 with curve $H_{mod}(s)$ (*2*): *a, b* — after optimization of cluster **6a4b8c** (*c*); *d, e* — after relaxation by the MD method during 8000 cluster steps **6a4b8c** (*f*).

are compared with the experimental curves for sample NC-1 in Figure 6.

Comparison of curves $H(s)$ calculated for NC-1 and for cluster **6a4b8c** has shown that maxima (200) and (004)

Table 4. Percentage of clusters in the final model for the structure of sample NC-1

Model consisting of clusters with sizes	Concentration, %	Energy, kcal/mol
6**a**4**b**8**c**	25.6	32 188
6**a**4**b**8**c*** (Figure 7, *c*)	8.5	3396
6**a**4**b**8**c** after 5000 MD steps	8.5	12 467
6**a**4**b**8**c** after 8000 MD steps (Figure 7,*f*)	17.1	11 766
2**a**2**b**2**c***	8.5	213
2**a**2**b**4**c***	8.5	405
4**a**4**b**7**c***	12.8	2116
6**a**4**b**8**c*** with „voids“ (Figure 8, *c*)	8.5	3365
8**a**8**b**8**c**	1.7	85 834

Note. * — clusters optimized by the Polak–Ribiere method.

(Figure 6, *b*) coincide in position, but differ in intensity: maximum at $s \sim 1.6\,\text{Å}^{-1}$ on curve $H_{mod}(s)$ is 2.2 times higher than the experimental one, maximum at $s \sim 2.4\,\text{Å}^{-1}$ is 3 times higher. Also, in the area of experimental diffusion maxima at $s \sim 5.6$ and $9\,\text{Å}^{-1}$, much narrower oscillations are observed than on experimental $H(s)$, i.e. the cluster structure is more ordered than the sample structure.

As described in Section 1.3, the Polak–Ribiere and MD methods were used for „amorphization“ of this cluster. Figure 7 demonstrates the obtained patterns of scattering by a cluster optimized by the Polak–Ribiere method and curve $H(s)$ after relaxation during 8000 steps by the MD method compared with the experimental scattering pattern obtained for sample NC-1.

After geometrical optimization by the Polak–Ribiere method (Figure 7, *c*), there are minor changes in the structure of initial cluster 6**a**4**b**8**c** built from the refined theoretical model of cellulose $I\beta$.

MD process (Figure 7,*f*) gives a more marked difference: there is significant deformation of elementary fibrils at the cluster interface, fibril reorientation within the model is also observed as the number of steps increases.

Figure 7 shows that both the Polak–Ribiere optimization and MD relaxation lead to a drastic decrease in oscillations by $H_{mod}(s)$ and, consequently, to a larger correlation with the experiment. However, position of the first maximum (Figure 7, *e*) shifts to smaller values of s as a result of cluster relaxation.

From comparison of Figure 5, 7, *c* and *d* it follows that the Polak–Ribiere leads to mutual disorientation of molecules (molecule twisting). As a result of MD relaxation, the initial structure gets very much disordered.

At the next simulation stage, initial cluster 6**a**4**b**8**c** was changed by removing a part of fibrils within the cellulose matrix as shown in Figure 8, *c*. This technique has been used earlier in building the nitrocellulose model in [31].

Comparison of Figures 7 and 8 shows that curves $H_{mod}(s)$ for a cluster with voids correlate better with the experiment than the optimized curves shown in Figure 7. Differences in curves $H_{mod}(s)$ and $H_{exp}(s)$ (Figure 8) are noticeable in the intensity and width of maximum (200) (Figure 8, *b*) and in the separation of maximum (004) at $H_{mod}(s)$.

On the assumption that the cellulose structure model can consist of a combination of clusters with various sizes and degree of deformation, rather than of the same fragments, it was proposed to consider clusters with sizes: 1**a**1**b**5**c**, 2**a**2**b**2**c**, 2**a**2**b**4**c**, 5**a**5**b**5**c** and so on, before and after the geometrical optimization.

Form of curves $I_{mod}(s)$ and $H_{mod}(s)$ calculated for each cluster was analyzed, and the fitting method (equation (4)) was used to find the percentage of clusters in the final model (Table 4), at which curves $I_{mod}(s)$ and $I_{exp}(s)$ had the smallest difference $R_p = 14\,\%$ (Figure 9).

Experimental maximum (200) at $s \sim 1.6\,\text{Å}^{-1}$ is adequately described by theoretical curve $I_{mod}(s)$ (Figure 9, *c*) and $H_{mod}(s)$ (Figure 9, *a*). Amorphous phase scattering also occurs on dependence $I_{mod}(s)$. Values of the model curve at s from 1.7 to $2.3\,\text{Å}^{-1}$ approach the experimental ones. Curve $H_{mod}(s)$ also approaches the experimental curve: maxima $s \sim 1.6\,\text{Å}^{-1}$ of the model and experimental curves almost coincide (Figure 9, *a*), maximum (004) on $H_{mod}(s)$ is as close to the experimental value as possible. Curves $W(r)$ (Figure 9, *d*) are well correlated: maxima at $r \sim 1.5$, 2.5, 2.8 and 3.7 Å agree with experimental values in positions and intensity, at $r \sim 4.5$ Å oscillation attenuation on curves $W(r)$ is observed.

Final model consists of $\sim 27\,\%$ of the crystalline component: clusters 6**a**4**b**8**c** and 8**a**8**b**8**c**; $\sim 26\,\%$ of amorphous-crystalline component with prevailing amorphous component: MD-relaxed clusters; clusters partially disordered by the Polak–Ribiere optimization: cluster with sizes 6**a**4**b**8**c** (with and without voids) $\sim 17\,\%$, and optimized smaller clusters (2**a**2**b**2**c**, 2**a**2**b**4**c**, 4**a**4**b**7**c**) $\sim 30\,\%$. The obtained

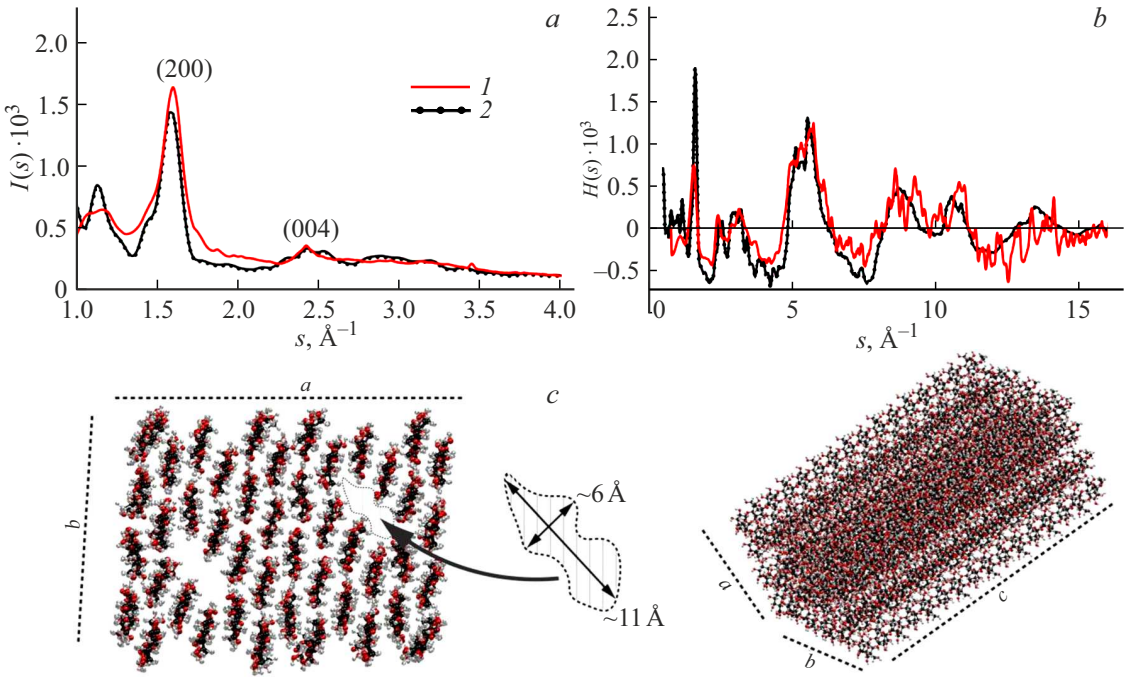

Figure 8. Scattering intensity distribution curves $I(s)$ (a) and s-weighted interference functions $H(s)$ (b) built for NC-1 (1) and for cluster 6**a**4**b**8**c** after removal of four elementary fibrils (c) (2).

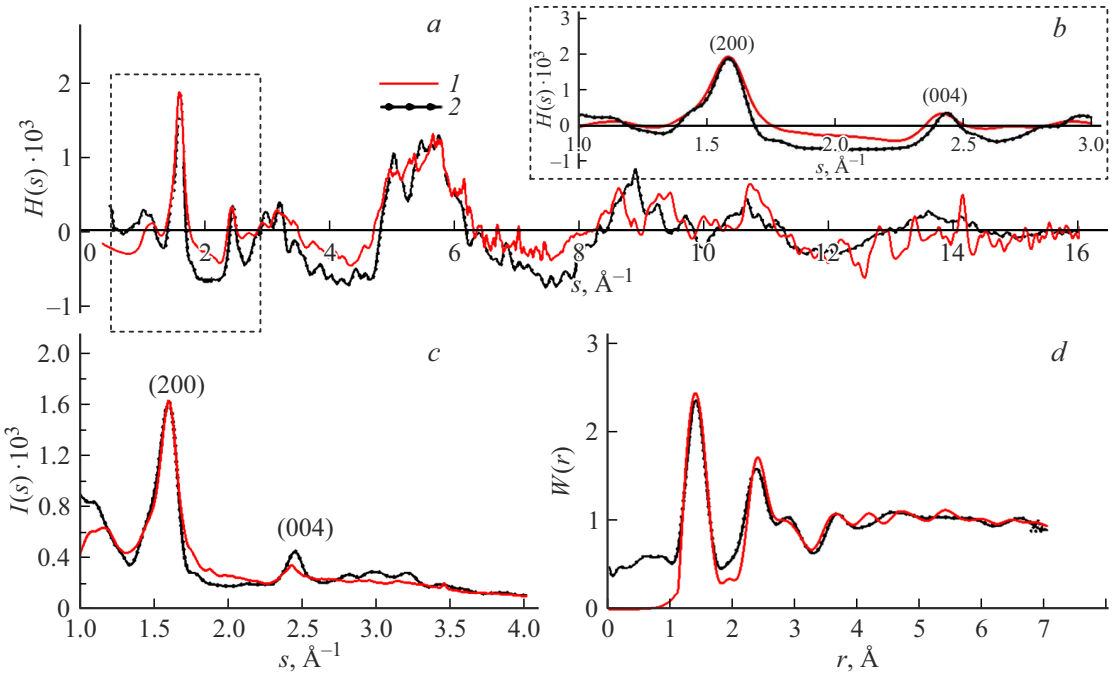

Figure 9. Comparison of s-weighted interference functions $H(s)$ (a, b), scattering intensity distribution curves $I(s)$ (c) and radial atom distribution functions $W(r)$ (d) built for NC-1 (1) and for model (2).

results are in good agreement with CD calculated for sample NC-1 (Table 2).

2.2.2. Sample NC-2

The same work was done for sample NC-2. Cluster 6**a**4**b**8**c** was used as a basis according to data obtained in Table 2. Figure 10 compares theoretical curves $I_{mod}(s)$, $H_{mod}(s)$ and $W_{mod}(r)$ for the final model with corresponding experimental curves. Uncertainty factor was $R_p = 22\,\%$. Percentage of clusters in the final model is shown in Table 5.

Scattering intensity distribution curves are qualitatively similar (Figure 10, c). $I_{mod}(s)$ has amorphous component distribution at $s \sim 1.6$ Å^{-1}, model maximum (200) agrees

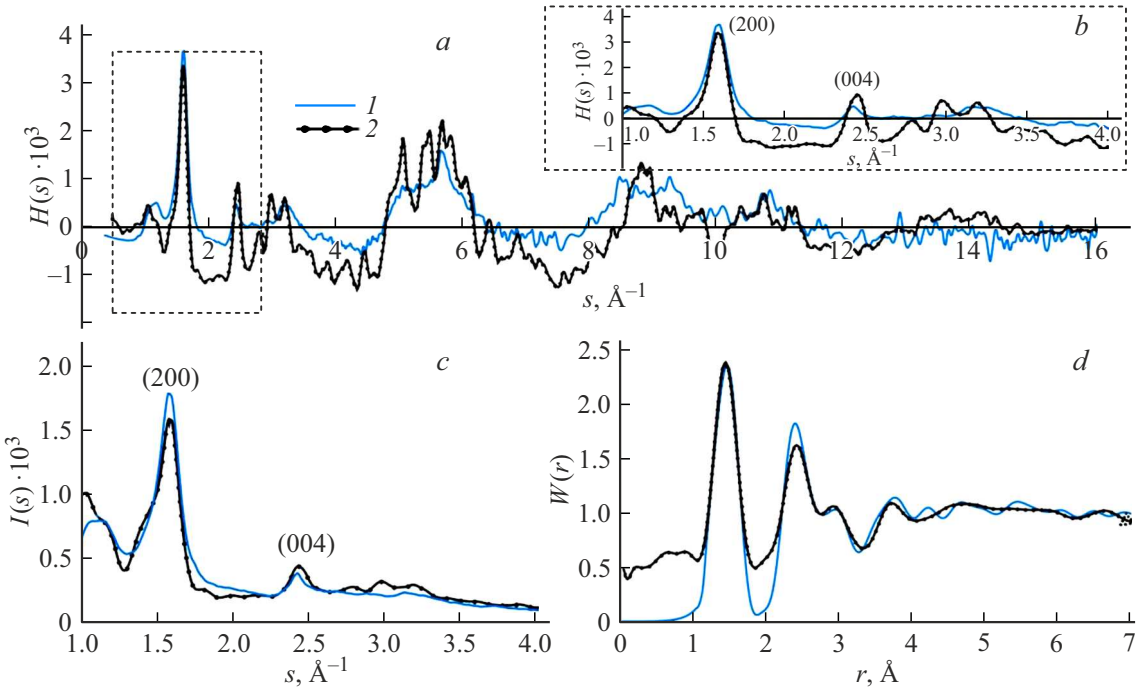

Figure 10. Curves $H(s)$ (a, b), $I(s)$ (c) and $W(r)$ (d) for NC-2 (1) and for model (2).

Table 5. Percentage of clusters in the final model for the structure of sample NC-2

Model consisting of clusters with sizes	Concentration, %	Energy, kcal/mol
6a4b8c	29.6	33 101
6a4b8c*	7.4	3459
6a4b8c after 5000 MD steps	14.8	3156
6a4b8c after 8000 MD steps	14.8	12 514
2a2b2c*	7.4	213
2a2b4c*	7.4	212
6a4b8c* with „voids“	14.8	3658
8a8b8c	3.7	167 945

Note. * — clusters optimized by the Polak–Ribiere method.

with the experimental one. Difference is only observed in the intensity of maximum at $s \sim 1.6$ Å^{-1}. Curves $W(r)$ are characterized by strongly pronounced maxima at $r \sim 1.6$ and $\sim$ 2.4 Å, $\sim$ 2.8 and 3.7 Å.

The final model consists of $\sim 33\,\%$ of the crystalline component: clusters **6a4b8c** and 8**a8b8c**; $\sim 30\,\%$ of amorphous-crystalline component with prevailing amorphous component:MD-relaxed clusters (at 5000 and 8000 steps); clusters partially disordered by the Polak–Ribiere optimization: cluster with sizes **6a4b8c** (with and without voids) $\sim 22\,\%$, and optimized smaller clusters (2a2b2c, 2a2b4c) $\sim 15\,\%$. Consequently, CD of the final model is $\sim 50\,\%$–$60\,\%$, which agrees with the data in Table 2.

Thus, the obtained results have shown the differences between the structures of nanocellulose samples extracted from DIP using the mineral acid hydrolysis and from powder celluloses obtained from waste linen fibers.

Conclusion

Structure of powder nanocellulose samples obtained from waste paper and cardboard DIP is characterized by cellulose phase $I\beta$. Degree of crystallinity of samples is $\sim 64\,\%$, which is much smaller than for cellulose extracted from plant feedstock. Coherent scattering region sizes of samples vary depending on the crys-

tallographic direction. The longest length is observed along the [001] fibril growth axis. Computer simulation method confirmed the presence of amorphous areas in the structure of samples NC-1 and NC-2: $\sim 26\,\%$ and $\sim 30\,\%$ — amorphous-crystalline component (using the MD method); $\sim 17\,\%$ and $\sim 22\,\%$ — component partially disordered by the Polak–Ribiere optimization; $\sim 30\,\%$ and $\sim 15\,\%$ — amorphous-crystalline component from small clusters, respectively. Optimized description of experimental data is achieved with superposition of several models with various ordering levels. Structural models of nanocellulose consisting of a combination of clusters with various sizes and degrees of deformation were first calculated.

Funding

This study was supported by grant No. 25-22-00475 from the Russian Science Foundation (https://rscf.ru/en/project/25-22-00475/).

Conflict of interest

The authors declare no conflict of interest.

References

[1] N. Lasrado, J. Reddy. Rev. Med. Virol., **30** (6), 1 (2020). DOI: 10.1002/rmv.2131
[2] K. Oksman, Y. Aitomäki, A.P. Mathew, G. Siqueira, Q. Zhou, S. Butylina, S. Tanpichai, X. Zhou, S. Hooshmand. Compos. Part A Appl. Sci. Manuf., **83**, 2 (2016). DOI: 10.1016/j.compositesa.2015.10.041
[3] E.C. Emenike, K.O. Iwuozor, O.D. Saliu, J. Ramontja, A.G. Adeniyi. Carbohydr. Polym. Technol. Appl., **6**, 100337 (2023). DOI: 10.1016/j.carpta.2023.100337
[4] Z. Li, D.A. Hensher, B. Zhou. Data Sci. Manag., **1** (1), 1 (2021). DOI: 10.1016/j.dsm.2020.12.001
[5] R.H. Atalla, D.L. Vanderhart. Solid State Nucl. Magn. Reson., **15** (1), 1 (1999). DOI: 10.1016/S0926-2040(99)00042-9
[6] M.H. Hussin, D. Trache, C.T.H. Chuin, et al. In *Sustainable Polymer Composites and Nanocomposites,* ed. by Inamuddin et al. (Springer Nature, Switzerland AG, 2019), p. 37. DOI: 10.1007/978-3-030-05399-4_2
[7] D.E. Ciolacu, F. Ciolacu, V.I. Popa. Cellulose Chem. Technol., **45** (1–2), 13 (2011).
[8] Y. Nishiyama, J. Sugiyama, H. Chanzy, P. Langan. J. Am. Chem. Soc., **125** (47), 14300 (2003). DOI: 10.1021/ja037055w
[9] A.M. Mikhailidi, Sh. Karim Saurov, V.I. Markin, N.E. Kotelnikova. Khimiya rastitel'nogo syr'ya, **27**, 2018 (2013) (in Russian).
[10] P. Lu, Y.-L. Hsieh. Carbohydr. Polym., **82** (2), 329 (2010). DOI: 10.1016/j.carbpol.2010.04.073
[11] Y. Habibi, L.A. Lucia, O.J. Rojas. Chem. Rev., **110** (6), 3479 (2010). DOI: 10.1021/cr900339w
[12] S. Beck-Candanedo, M. Roman, D.G. Gray. Biomacromolecules, **6** (2), 1048 (2005). DOI: 1021/bm049300p
[13] M. Rajinipriya, M. Nagalakshmaiah, M. Robert, S. Elkoun. ACS Sustainable Chem. Eng., **6** (3), 2807 (2018). DOI: 10.1021/acssuschemeng.7b03437
[14] T. Owoyokun, C.M. Pérez Berumen, A. Martínez Luévanos, et al. Biointerface Res. Appl. Chem., **11** (4), 11797 (2021). DOI: 10.33263/BRIAC114.1179711816
[15] W.W. Ruland. Acta Cryst., **14**, 1480 (1961). DOI: 10.1107/S0365110X61003429
[16] M.A. Torlopov, V.I. Mikhaylov, E.V. Udoratina, L.A. Aleshina, A.I. Prusskii, N.V. Tsvetkov, P.V. Krivoshapkin. Cellulose, **25**, 1031 (2018). DOI: 10.1007/s10570-017-1624-z
[17] D.A. Yatsenko, T.B. Medvedeva. Zhurnal strukturnoi chimii (in Russian). **60** (9), 1460 (2019). DOI: 10.26902/JSC_id46197
[18] A. Thygesen, J. Oddershede, H. Lilholt, A.B. Thomsen, K. Stahl. Cellulose, **12**, 563 (2005). DOI: 10.1007/s10570-005-9001-8
[19] L.A. Aleshina, O.N. Shivrin. *Rentgenovsky analiz kristallov. Neoriya i rezultaty difraktsionnykh issledovaniy* (Palmarium Academic Publishing, Republic of Moldova, 2012)
[20] M. Khandelwal, A.H. Windle, N. Hessler. J. Mater. Sci., **51**, 4839 (2016). DOI: 10.1007/s10853-016-9783-0
[21] M. Khandelwal. *Structure and processing of fibrous cellulose: bacterial and ascidian material* (doctoral thesis, Apollo — University of Cambridge Repository, 2013), DOI: 10.17863/CAM.14271
[22] K. Cheng, J. Catchmark, A. Demirci. J. Biol. Eng., **3** (12), 1 (2009). DOI: 10.1186/1754-1611-3-12
[23] S.K. Saurov, K. Svedström, N. Kotelnikova. Cellulose Chem. Technol., **53** (9), 885 (2019). DOI: 10.35812/CelluloseChemTechnol.2019.53.86
[24] L.A. Aleshina, A.D. Fofanov. *rentgenostrukturny analiz amorfnykh materialov* (Izd-vo „PetrGU", Petrozavodsk, 1987) (in Russian)
[25] Programma „Metod Ritvelda" № 2006610292 ot 27.03.2006, Programmny kompleks PDWin 4.0. NPO „Burevestnik", SPb., (2004) (in Russian)
[26] C. Driemeier. Cellulose, **21**, 1065 (2014). DOI: 10.1007/s10570-013-9995-2
[27] A.I. Prusskii, L.A. Aleshina. Polymer Sci. Ser. A, **58**, 386 (2016). DOI: 10.1134/S0965545X16030147
[28] O. Borgen, Chr. Finbak. Acta Chem. Scand., **8**, 829 (1954).
[29] B.E. Warren. *X-ray Diffraction* (Addison–Wesley, Reading, MA, 1969)
[30] D.V. Gromyko, A.I. Prusskii, O.V. Tokko, N.E. Kotel'nikova. Russ. J. Bioorg. Chem., **50** (7), 2765 (2024). DOI: 10.1134/S1068162024070197
[31] A.I. Prusskii, L.A. Aleshina, I.V. Lyukhanova, O. Sidorova, V. Budaeva, G.V. Sakovich. Polymer Sci. Ser. A, **64**, 733 (2022). DOI: 10.1134/S0965545X22700481
[32] C.S. Tsai. *Introduction to Computational Biochemistry* (Wiley-Liss, NY., 2002)
[33] C.H. Haigler, M.J. Grimson, J. Gervais, N. Le Moigne. PLoS ONE, **9** (4), e93981 (2014). DOI: 10.1371/journal.pone.0093981
[34] A.D. Fofanov. V sb.: *Fiziko-khimicheskie metody izucheniaya mineralnykh agregatov, mineraloidov i sinteticheskikh materialov: problemy i perspektivy,* pod red. V.V. Kovalevskogo, S.V. Egorovoy, E.N. Svetovoy, A.D. Fofanova (KarNTs RAN, Petrozavodsk, 2018), s. 73.(in Russian)

[35] A.D. French, P.S. Howley. In *Cellulose and Wood — Chemistry and Technology,* ed. by C. Schuerch (Wiley, NY., 1989), p. 159.
[36] E.A. Tchernova, L.A. Aleshina, N.E. Kotelnikova. V cb.: *Struktura i fiziko-khimicheskie svoistva tsellyuloz i nanokompozitov na ikh osnove,* pod red. N.E. Kotelnikovoy, R.N. Osaulenko, L.A. Aleshinoy, S.V. Loginivoy (Nauchno-innovatsionnyi tsentr, Krasnoyarsk, 2016), s. 81.(in Russian) DOI: 10.12731/nkras.ru/SFHS.2016.164

Translated by E.Ilyinskaya